Image Segmentation Based on Fuzzy Connectedness Using Dynamic Weights*

Amol S. Pednekar and Ioannis A. Kakadiaris

Department of Computer Science
University of Houston
Houston, TX, 77204, USA
http://www.cs.uh.edu

Technical Report Number UH-CS-05-13

July 6, 2005

Keywords: Image segmentation, Fuzzy Connectedness, Dynamic Weights.

Abstract

Traditional segmentation techniques do not quite meet the challenges posed by inherently *fuzzy* medical images. Image segmentation based on fuzzy connectedness addresses this problem by attempting to capture both closeness, based on characteristic intensity, and "hanging togetherness", based on intensity homogeneity, of image elements to the target object. This paper presents a modification and extension of previously published image segmentation algorithms based on fuzzy connectedness, which is computed as a linear combination of an object-feature based and a homogeneity based component using fixed weights. We provide a method, called DyW (fuzzy connectedness using *Dy*namic *W*eights), to introduce directional sensitivity to the homogeneity based component and to dynamically adjust the linear weights in the functional form of fuzzy connectedness. Dynamic computation of the weights relieves the user of the exhaustive search process to find the best combination of weights suited to a particular application. This is critical in applications such as analysis of cardiac cine Magnetic Resonance (MR) images, where the optimal combination of affinity component weights can vary for each slice, each phase, and each subject, in spite of data being acquired from the same MR scanner with identical protocols. We present selected results of applying DyW to segment phantom images and actual MR, Computed Tomography, and infrared data. The accuracy of DyW is assessed by comparing it to two different formulations of fuzzy connectedness. Our method consistently achieves accuracy of more than 99.15% for a range of image complexities: contrast 5% to 65%, noise-to-contrast ratio (NCR) of 6% to 18%, and bias field of four types with maximum gain factor of up to 10%.

*This work was supported in part by the NSF under Grants IIS–0431144, IIS–0335578 and IIS–9985482. Any opinions, findings, and conclusions or recommendations expressed in this material are those of the authors and do not necessarily reflect the views of the NSF.

Image Segmentation Based on Fuzzy Connectedness Using Dynamic Weights*

Amol S. Pednekar and Ioannis A. Kakadiaris

Abstract

Traditional segmentation techniques do not quite meet the challenges posed by inherently *fuzzy* medical images. Image segmentation based on fuzzy connectedness addresses this problem by attempting to capture both closeness, based on characteristic intensity, and "hanging togetherness", based on intensity homogeneity, of image elements to the target object. This paper presents a modification and extension of previously published image segmentation algorithms based on fuzzy connectedness, which is computed as a linear combination of an object-feature based and a homogeneity based component using fixed weights. We provide a method, called DyW (fuzzy connectedness using *Dy*namic *W*eights), to introduce directional sensitivity to the homogeneity based component and to dynamically adjust the linear weights in the functional form of fuzzy connectedness. Dynamic computation of the weights relieves the user of the exhaustive search process to find the best combination of weights suited to a particular application. This is critical in applications such as analysis of cardiac cine Magnetic Resonance (MR) images, where the optimal combination of affinity component weights can vary for each slice, each phase, and each subject, in spite of data being acquired from the same MR scanner with identical protocols. We present selected results of applying DyW to segment phantom images and actual MR, Computed Tomography, and infrared data. The accuracy of DyW is assessed by comparing it to two different formulations of fuzzy connectedness. Our method consistently achieves accuracy of more than 99.15% for a range of image complexities: contrast 5% to 65%, noise-to-contrast ratio (NCR) of 6% to 18%, and bias field of four types with maximum gain factor of up to 10%.

Index Terms

Image segmentation, Fuzzy Connectedness, Dynamic Weights.

I. Introduction

Medical image computing has revolutionized the field of medicine by providing novel methods to extract and visualize information from medical data acquired using various acquisition modalities. Image segmentation is one of the most important steps in the higher level analysis of preprocessed patient image data, and can aid in diagnosis, functional categorization, and prognosis, as well as evaluation of therapeutic interventions. The main goal of the image segmentation process is to divide an image into parts that have a strong correlation with objects or areas of the real world depicted in the image. When the object or region of interest has intensity features significantly different from the rest of the image, it is often possible to threshold the region of interest to produce a binary image.

However, medical images are not incisive; they are characterized by a composition of small differences in signal intensities between different tissue types, noise, blurring, background variation, partial voluming, and certain acquisition-specific effects, e.g., surface coil intensity falloff in Magnetic Resonance imaging (MRI). Ambiguities and uncertainties are introduced in image formation due to approximations made during image acquisition, limited spatial, temporal, and parametric resolutions, heterogeneous tissue composition of the human body, in addition to movement of the subject. This imprecision makes it extremely difficult to determine the exact location of the boundary points of the object of interest purely based on the intensity values assigned to the individual image elements.

Nevertheless, anatomical objects in medical data are characterized by certain intensity level and intensity homogeneity features. The image elements seem to "hang together" to form a certain perception of the object region. Thus, medical image segmentation would benefit from a method based on the "hanging togetherness" property of the object of interest. The image segmentation framework based on Fuzzy Connectedness developed by Udupa and

*This work was supported in part by the NSF under Grants IIS–0431144, IIS–0335578 and IIS–9985482. Any opinions, findings, and conclusions or recommendations expressed in this material are those of the authors and do not necessarily reflect the views of the NSF.

his collaborators [1] effectively captures the "hanging togetherness" of image elements specified by their strength of fuzzy connectedness. Fuzzy connectedness is constructed by combining an object-feature based and a homogeneity based affinity component in a fixed manner with various functional forms [2]. The best combination of affinity component weights for a particular functional form and particular application is determined by performing an exhaustive search.

In applications involving a large number of studies based on a fixed image acquisition protocol, the affinity parameters and the threshold may be fixed without requiring per-case adjustment. However, without the same protocol-specific tissue indication for intensity values, it becomes very difficult to set values for the affinity parameters and the threshold in a manner independent of patient studies. Cardiac cine MR images as an example pose numerous challenges. MRI generally requires several cycles of signal generation followed by signal measurement. Thus, any motion of tissues between the excitation cycles causes blurring and other motion artifacts. The heart-motion and respiration cause a shift in the overall position of the heart throughout the image acquisition process. In addition, uneven breath holding and patient motion introduce further artifacts. Thus, the quality of cardiac cine-MR relies on the ability of the operator and scanner to compensate for these changes and the ability of the post-processor to rectify the intensity falloff in surface coil MRI. In general, the blood intensity value (object-feature) varies from the base to apex of the heart in every slice in the same phase of the cardiac cycle without any generic pattern of variation within a single patient. Furthermore, the blood pool intensity (homogeneity) changes within a slice due to partial voluming, while anatomical features like papillary muscles and valves cause blood flow artifacts.

Thus, in this application area, the optimal combination of the affinity component weights and the threshold for the connectivity scene varies for each slice, each phase, and each patient in spite of the data being acquired from the same MR scanner with identical protocol. As a result, precision, accuracy, and efficiency of segmentation may be compromised [3]. It may be necessary to adjust the parameters for each study to handle image-dependent variations in intensity. Our goal is to relieve the user from the task of selection or computation of these affinity component weights while preserving the quality of segmentation achieved using the framework based on fuzzy connectedness, by providing a method to dynamically adjust the weights of the two affinity components in the linear functional form of fuzzy connectedness. In addition, we introduce directional sensitivity to the homogeneity based component to account for directional background inhomogeneity (e.g., bias field in MR). We call this image segmentation method DyW (fuzzy connectedness using *Dy*namic *W*eights).

The remainder of this paper is organized as follows. In Section II, we provide a brief overview of image segmentation methods based on fuzzy connectedness. In Section III, we provide the particular fuzzy connectedness framework that we employ, and in Section IV we explain our modifications to this framework and describe DyW in detail. In Section V, we present results of an evaluation study of DyW on synthetic phantom data, a comparison of results using two other functional forms of fuzzy connectedness, and results obtained on real medical data acquired using different imaging modalities. Section VI concludes by summarizing our findings.

II. Previous Work

The challenges in analyzing medical image data encouraged researchers to develop segmentation algorithms which regard regions as fuzzy subsets of the image, where an image data element may be classified partially into multiple potential classes. The theory of fuzzy sets [5] is believed to effectively model the fuzziness of medical image data. However, apart from fuzzy classification, segmentation needs to address the intensity inhomogeneities within an object of interest. The fuzzy geometrical connectedness approach added spatial measures to handle the spatial uncertainties in the images [6], [7]. Fuzzy connectedness represented an important topological property of images. In addition, "hanging togetherness" was incorporated in the same fuzzy settings [8], [9].

The notion of a fuzzy object, based on ideas of fuzzy connectedness of image elements in an n-dimensional digital space for image segmentation was first developed by Udupa and Samarasekera [1]. This fuzzy-connectedness based image segmentation framework effectively captures the fuzzy "hanging togetherness" of image elements specified by their strength of connectedness. Specifically, a fuzzy connectedness between two image elements is computed based on their spatial nearness as well as the similarity of their intensity based features, which captures the local hanging togetherness of image elements. The global fuzzy connectedness between any two spatial elements (spels) in the image considers the strengths of all possible paths between them, where the strength of a particular path is

Parts of this work have appeared in [4].

the weakest affinity between the successive pairs of spels along the path. Thus, the strongest connectedness path between any two spels specifies the degree of hanging togetherness between them. The fuzzy extent of an object is computed by expanding it from the initial seed points based on this global fuzzy connectedness.

This framework was further extended with the introduction of object scale, which allowed the size of the neighborhood to be changed in different parts of the image and the introduction of a variety of functional forms for each affinity component separately [2]. In the relative fuzzy connectedness approach, all the important objects in the image are allowed to compete among themselves to seize the membership of image elements based on their relative strength of connectedness to reference elements [10]. The fuzzy-connectedness based image segmentation framework was also generalized for the identification of multiple elements in an image [11]. A recent approach using tensor scale in affinity computation allows for an effective utilization of local size, orientation, and anisotropy in a unified manner [12].

In previous approaches, connectedness, in general, consists of three major affinity components: 1) spel adjacency, 2) intensity homogeneity, and 3) object-feature. One may devise a variety of functional forms for each component separately and combine them to the affinity relation suited for a specific application [2]. To effectively capture the degree of local hanging togetherness of the spels, both the homogeneity and object-feature based components should be considered in the design of fuzzy spel affinities. However, in the previous approaches the homogeneity and object-feature based components are treated totally independent of each other. The functional forms and the parameters associated with these components allow many possible choices for fuzzy spel affinities. Saha *et al.* [2] conducted experimental studies for obtaining an insight into the best choices. One of the shortcomings of these approaches is the need for determination of optimal affinity parameters and the threshold for the connectivity scene (Note: In relative fuzzy connectedness, the need for a threshold is obviated).

III. A Framework for Fuzzy Connectedness

A. Preliminaries

A minimal set of terminology and definitions are presented to provide the preliminaries of the fuzzy connectedness formulation we employ. We follow the terminology of Udupa *et al.* [1], [2].

Let X be any reference set. A *fuzzy* subset $\mathcal{A}$ of X is a set of ordered pairs $\mathcal{A} = \{(x, \mu_{\mathcal{A}}(x))|\ x \in X\}$, where $\mu_{\mathcal{A}} : X \rightarrow [0, 1]$ is the *membership function* of $\mathcal{A}$ in X (μ is subscripted by the fuzzy subset under consideration). A *fuzzy* relation ρ in X is a fuzzy subset of $X \times X$. We shall call a fuzzy relation ρ in X that is reflexive ($\forall x \in X, \rho(x, x) = 1$) and symmetric ($\forall x, y \in X, \rho(x, y) = \rho(y, x)$) a *proximity* in X, and the pair (X, ρ) a *fuzzy space*. Let $X = \mathbf{Z}^n$, the set of n-tuples of integers. A proximity α in $\mathbf{Z}^n$ is called an *adjacency* and the pair $(\mathbf{Z}^n, \alpha)$ is called a *digital* fuzzy space. The concept of fuzzy digital space characterizes the underlying digital grid independent of any image related concepts, and it is desirable that μ_α is a non-increasing function of the distance in $\mathbf{Z}^n$. In this fuzzy digital space, any scalar function $f : C \rightarrow [L, H]$ from a finite subset C of $\mathbf{Z}^n$ to a finite subset $[L, H]$ of the integers defines a *scene* (C, f) over $(\mathbf{Z}^n, \alpha)$. In a scene (C, f), a proximity κ in C is called an *affinity*. An affinity relation K is called a *similitude* if it is also transitive: $\forall x, z \in C, \mu_K(x, z) = \max_{y \in X}\{\min\{\mu_K(x, y), \mu_K(y, z)\}\}$.

Starting from any affinity κ in C, and using the notion of *path strength*, one can construct a similitude K in C, called κ–connectedness and denoted by the upper case form of the symbol used for the corresponding affinity. A *path* p_{xy} from x to y in C is a sequence of $m \geq 2$ elements of C, not necessarily distinct, such that $p_{xy} = \{x = x^{(1)}, x^{(2)}, ..., x^{(m)} = y\}$. Each pair $(x^{(i)}, x^{(i+1)})$ is a *link* in the path. The set of all paths in X between x and y is denoted by P_{xy}. The *strength* μ of each link $(x^{(i)}, x^{(i+1)})$ in a path p_{xy} is simply the affinity $\mu_\kappa(x^{(i)}, x^{(i+1)})$. The *strength* of connectivity along a path p_{xy} is determined by its weakest link, namely: $\mu(p_{xy}) = \min\{\mu_\kappa(x^{(1)}, x^{(2)}), \mu_\kappa(x^{(2)}, x^{(3)}), ..., \mu_\kappa(x^{(m-1)}, x^{(m)})\}$. The fuzzy κ-connectedness of x and y is the strength of the strongest path in P_{xy}: $\mu_K(x, y) = \max_{p_{xy} \in P_{xy}}\{\mu(p_{xy})\}$. (Note: P_{xy} is an infinite set, but the use of $\max$ instead of $\sup$ is justified since a scene is a finite subset of $\mathbf{Z}^n$ and thus $\mu(p_{xy})$ can only assume a finite number of values). The relation K is a similitude relation in C [1].

Given a κ–connectedness similitude K in a scene (C, f) and a specific scene element o, the κ–connectedness scene (C, f_{K_o}) is defined by $f_{K_o}(c) = \mu_K(o, c)$ for all c in C. This defines a family of equivalence relations in C, since the relation defined by $K_\theta = \{(o, c)|\mu_K(o, c) \geq \theta\}$ is an equivalence relation for any threshold $\theta \in [0, 1]$. Thus, segmentation of the initial scene (C, f) results from thresholding this final scene (C, f_{K_o}) at a selected κ–connectedness level [1].

B. Fuzzy Affinity

For the sake of simplicity and clarity of exposition, we restrict our presentation to the two–dimensional (2D) case, but our method is not dimension–specific. This is because we follow the framework of Udupa *et al.* [1], [2], so the extension to three or higher dimensional problems is straightforward.

For processing of 2D data, the fuzzy digital space is $(\mathbf{Z}^2, \alpha)$, where

$$\mu_\alpha(c,d) = \begin{cases} 1, & \text{if } \sqrt{\sum_{i=1}^{2}(c_i - d_i)^2} \leq 1 \\ 0, & \text{otherwise} \end{cases}$$

the scene (C, f) represents acquired image data, and (c, d) is a pair of pixels in this scene. The generic form of an affinity relation μ_κ between c and d is given by [1]:

$$\mu_\kappa(c,d) = h\left(\mu_\alpha(c,d), f(c), f(d), c, d\right),$$

where h is a scalar-valued function with range $[0, 1]$. In this general form $\mu_\kappa(c, d)$ may be shift variant, meaning it may depend on the locations of pixels c and d.

It was recognized early on that there should be two specific, shift-invariant components of affinity in this design – μ_ψ, which is based on *homogeneity* and μ_ϕ, which is based on *object–features* [2]. The two components can be combined in the following generic functional form for μ_κ:

$$\mu_\kappa(c,d) = \mu_\alpha(c,d) g\left(\mu_\phi(c,d), \mu_\psi(c,d)\right),$$

where μ_ϕ is an affinity based on average intensity $I\left(f(c), f(d)\right) = \frac{f(c)+f(d)}{2}$ and μ_ψ is an affinity based on intensity homogeneity $D\left(f(c), f(d)\right) = |f(c) - f(d)|$.

The μ_ϕ component measures affinity based on average intensity I and describes how close the feature value (intensity) is to some specified object feature. As an example, a Gaussian function can be used:

$$\mu_\phi(c,d) = g_1 \circ I\left(f(c), f(d)\right),$$

where

$$g_1(t) = \exp\left(-\frac{1}{2}\left(\frac{t - m_1}{s_1}\right)^2\right)$$

and m_1 and s_1 are the mean and standard deviation of the intensity of the object to be segmented.

The μ_ψ component measures affinity based on intensity homogeneity D and describes how similar the intensity value stays within a region. Again, a Gaussian function provides an example:

$$\mu_\psi(c,d) = g_2 \circ D\left(f(c), f(d)\right),$$

where

$$g_2(t) = \exp\left(-\frac{1}{2}\left(\frac{t - m_2}{s_2}\right)^2\right)$$

and m_2 and s_2 are the mean and standard deviation of the intensity homogeneity of the object to be segmented.

There are several choices that have been proposed for the function g. The original is a simple linear combination [1]:

$$\mu_\kappa(c,d) = \omega_1 \mu_\phi(c,d) + \omega_2 \mu_\psi(c,d),$$

where $\omega_1 + \omega_2 = 1$. The more homogeneous the region to which c and d belong, the greater is the value of μ_ψ. On the other hand, μ_ϕ takes a high value when c and d are both close to the expected intensity value for the object. The weighted linear combination of these two components strives to effectively capture both the global connectedness and local hanging togetherness of the object to be defined.

Note that these components are considered independent of each other and the weights for these components are static. This assumes that the level of dominance of one component over the other is constant over the entire object. However, in scale-based fuzzy connectedness [2] there is some adaptivity of these components via the concept of local scale region and via the geometric mean formulation of affinity as $\mu_\kappa(c,d) = \mu_\alpha(c,d)\sqrt{\mu_\psi(c,d)\mu_\phi(c,d)}$.

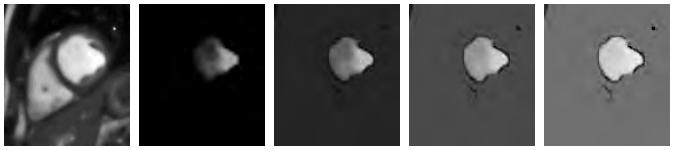

(a) (b) (c) (d) (e)

Fig. 1. Fuzzy affinity maps of a short-axis cardiac MR image (a), for which the weight for object-feature intensity (μ_ϕ)is set to (b) 1.0, (c) 0.75, (d) 0.50, and (e) 0.25, respectively.

IV. Modifications and Extensions to the Framework

In this section, we propose a modified functional form for μ_ψ, where directional sensitivity along with magnitude account for directional background inhomogeneity (e.g., bias field in MR). In addition, we discuss the dynamic determination of weights for μ_ψ and μ_ϕ in detail.

We start by providing some motivation, based on the field of MR imaging. Suppose, as in the case of MR, that the image of the object has a slow varying background intensity component in a horizontal direction. Then, pixels c and d that belong to the same object but are far apart from each other in the horizontal direction will have very different intensities. By increasing the weight for μ_ψ we can find a path between c and d such that the intensities of all the horizontal links on the path are similar enough to indicate the connectedness between c and d. However, this might create a path between pixels u and v which are vertically apart in the image, but belong to two different objects. This will happen because the increased weight for μ_ψ is tolerating the same amount of dissimilarity between the intensities in each vertical link. Figure 1 depicts how the affinities assigned to pixels vary with the change in value of ω_2. Thus, it is intuitive to treat path links differently depending on their direction and the characteristic magnitude of increase or decrease in object intensity in that direction. This suggests that weights for μ_ϕ and μ_ψ need to vary in accordance with the dominance of one affinity component over the other and the direction of links in the chain.

One way to address this problem is to assign the weights to μ_ϕ and μ_ψ components based on the relative degree of nearness of the link (c', d') in the respective component domains. In MR images, the intensity of the object changes gradually near the inter-object boundaries, making the boundaries diffused (for cardiac MR images, flow artifacts and partial voluming of blood with the heart wall and papillary muscles have the same effect). In these cases, even though the object-feature (characteristic intensity) is disparate near the object boundaries, the intensities of each link (c', d') may still be similar, resulting in increased weight for the intensity-homogeneity component μ_ψ. However, this may merge two objects when intensity change is very slow and gradual at the boundary [2]. This effect is counteracted by allowing the weight for μ_ψ to increase only to the point where $g_1 \circ I$ is still within 3σ from the characteristic object intensity. In the definition of μ_ϕ, $g_1 = 0.01$ corresponds to $3s_1$ distance from the characteristic intensity of the target object. Thus, dynamically computed weights for affinity components, along with a directionally sensitive μ_ψ, effectively capture the fuzzy extent of the object.

A. Directionally Sensitive Intensity Homogeneity for Fuzzy Affinity

In the original formulation of μ_ψ, the direction of intensity inhomogeneity and its sign are not taken into consideration. This type of formulation allows equal amounts of intensity dissimilarities in path links irrespective of the direction of the link and does not consider the increase or decrease in intensity across the link due to directional background variation. We propose to modify μ_ψ to be directionally sensitive by computing four different pairs (m_2, s_2) from the sample region, one for each of the four possible directions ($N \rightarrow S$), ($S \rightarrow N$), ($E \rightarrow W$) and ($W \rightarrow E$). The affinity μ_ψ on each link (c, d) is then computed using the (m_2, s_2) parameter pair computed in the direction of that link. The bias in intensity in a specific direction is thus accounted for by allowing different levels and signs of dissimilarities in different link directions. This modified relation is still an affinity because symmetry is preserved (since $m_2^{N \rightarrow S} = -m_2^{S \rightarrow N}$, and similarly for all the other compass directions).

B. Dynamic Weights for Fuzzy Affinity

The bias field and noise in an image can change the nearness of object pixels in terms of characteristic object intensity; however, the nearness may still be maintained in terms of intensity homogeneity. We have developed a

method to determine the weights for μ_ϕ and μ_ψ dynamically based on the level of dominance of one component over the other. We determine the level of dominance by the ratio of the two components. Specifically, we compute ω_1 and ω_2 as follows:

$$\omega_1 = \frac{g_1}{g_1 + g_2}, \text{ and } \omega_2 = 1 - \omega_1.$$

Thus, ω_1 becomes high in the regions of the image with intensity almost similar to the intensity of the object to be segmented in the scene. Conversely, in regions where intensity is different from the characteristic object intensity but intensity homogeneity is maintained, ω_2 is increased to capture the local chain homogeneity. However, when the object-based intensity $g_1 \circ I$ falls below 0.01 (i.e., $3s_1$), both ω_1 and ω_2 are set to zero, to avoid merging of different objects with similar intensity homogeneity.

C. The DyW algorithm

Starting with a small (5x5 pixels) sample region of the segmentation target as a seed, we compute (m_1, s_1), and the four pairs $(m_2^{N\to S}, s_2^{N\to S})$, $(m_2^{S\to N}, s_2^{S\to N})$, $(m_2^{E\to W}, s_2^{E\to W})$, and $(m_2^{W\to E}, s_2^{W\to E})$, which correspond to the four different compass directions. We then follow the dynamic programming based algorithm for the extraction of the κ-connectedness scene (C, f_{K_o}) as presented by Udupa and Samarasekera [1]. In order to objectively compute the best possible threshold level θ for segmentation, we use Otsu's automatic thresholding method [13]. This process is entirely objective and void of any user interaction or manipulation.

V. Results and Discussion

In this section, we present the performance of our DyW image segmentation method. First, we present the results of image segmentation using the DyW algorithm on a phantom data set to evaluate its robustness and accuracy. Then, we present the comparison of DyW with two different formulations of fuzzy connectedness, as the arithmetic (EqW) or geometric (Sqrt) mean of its affinity components μ_ϕ and μ_ψ. In particular, the *EqW* and *Sqrt* fuzzy connectedness similitudes are defined using the following fuzzy affinity formulations: $\mu_\kappa = \frac{1}{2}\mu_\phi + \frac{1}{2}\mu_\psi$, and $\mu_\kappa = \sqrt{\mu_\phi \mu_\psi}$, respectively. Finally, we present the results of applying DyW on actual MR, infrared, and Computed Tomography (CT) data.

One of the main challenges of evaluating segmentation algorithms on medical data is that the absolute ground truth cannot be defined. Testing a segmentation algorithm on a phantom data set allows for the establishment of a ground truth and the definition of an evaluation metric. The image quality depends on certain acquisition parameters of the imaging modality, such as spatial resolution, contrast sensitivity, noise to contrast ratio (NCR), and background intensity variations (bias).

Contrast is the basis for image perception and plays a vital role in defining the quality of the image. Image contrast is defined using the image intensities as $(|SA - SB|)/(SA + SB)$, where SA and SB are the luminance in the image regions A and B (background), respectively. The physics of image acquisition introduces variable contrast sensitivity for different tissue types. Noise is always present in image acquisition; most especially in medical image acquisition as a result of the inaccuracies imposed by the nature of the scanners. We use the NCR to quantify it in this paper (instead of contrast–to–noise) as NCR helps us introduce noise that is proportional to the contrast of the target object with respect to its neighborhood in the phantom image. Bias in MR images is a gradual change in intensity gain factor with respect to the position of the receptor coil. It causes the region of interest, if it is large enough, to exhibit significantly different intensity levels. For example, the left side of a region of interest may have intensity values considerably lower than the right side of the region. This causes a problem for most segmentation algorithms that are solely based on intensity-based features.

A computational phantom data set was developed, $P = \{\mathcal{C}_i | \mathcal{C}_i = (C, f_i), 1 \leq i \leq 400\}$, where each C_i is 128 x 128 pixels. Starting with this original synthetic 2D scene with a background intensity of zero, a total of 400 phantom images were created by introducing five different contrast levels, four varying degrees of zero-mean Gaussian white noise, five varying degrees of bias level, and four different types of bias fields. These variations will serve as the parameters to assess the robustness of the DyW method.

The pixels of the target region of the original synthetic 2D scene were assigned an intensity value of five different degrees of contrast level (0.65, 0.5, 0.35, 0.20 and 0.05) to generate five 2D scenes. The low values of contrast levels were selected to test extreme cases (representing medical images where neighboring tissue contrast is very small).

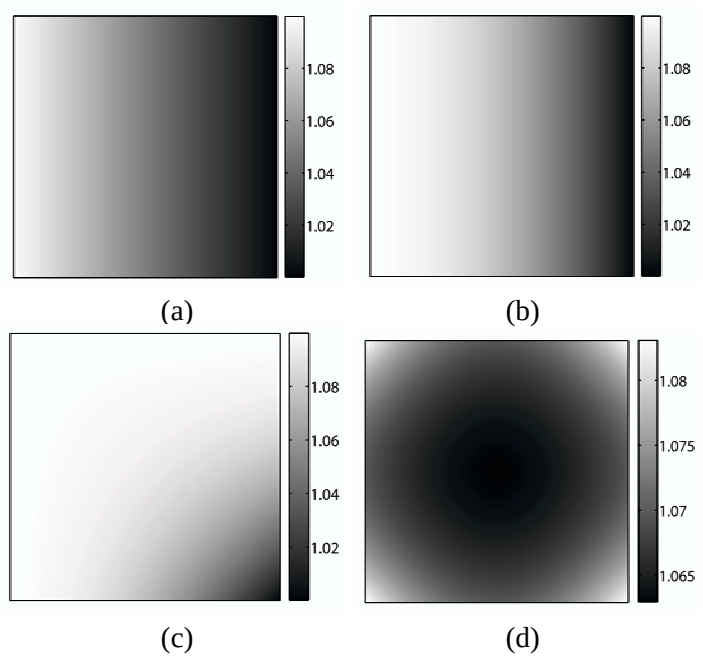

Fig. 2. Bias gain factors for four types of bias fields; (a) Type I, (b) Type II, (c) Type III, and (d) Type IV.

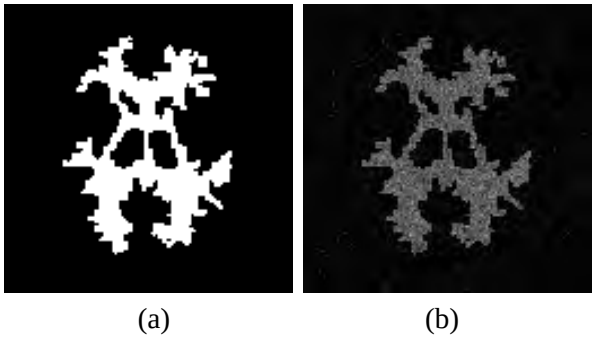

Fig. 3. Representative phantom images: (a) original, and (b) high bias field with high noise (contrast level $= 0.5$, bias level $= 10\%$, NCR $= 0.18$, Bias Type IV).

From this set of five simulated scenes, we created 20 2D scenes by independently adding four different levels of zero-mean correlated white Gaussian noise to each 2D scene. The variance of Gaussian noise was expressed in terms of NCR[2], where NCR ranges from 0.06 to 0.18 with increments of 0.04. Each of these twenty 2D scenes were independently multiplied by four different types of bias fields. The maximum gain factor of bias fields ranges from 0% to 10% with increments of 2.5% resulting in a total of 400 simulated 2D scenes.

The bias due to coil intensity falloff in MR is simulated as a linear combination of linear and second order ramp to capture gain factor as a function of distance from the receptor coil. The ramp type bias was defined as: $b(x, y) = \sum_0^1 \sum_0^1 f(x)f(y)$, where image coordinates x, y are scaled to the range $[0, 1]$ with $f(x) = x$ and $f(y) = 1$ (Type I), $f(x) = x^2$ and $f(y) = 1$ (Type II), and $f(x) = x^2$ and $f(y) = y^2$ (Type III). The Type IV bias was defined as equal weighted linear combination of four Type III bias fields rotated by 90^o to simulate bias field with four receiver coils located on the corners of the phantom image. The four types of bias fields are depicted in Figure 2. Figure 3 depicts examples from the phantom data set.

We evaluate and compare the DyW algorithm with the EqW and Sqrt algorithms using the three measures of accuracy recommended by Udupa *et al.* [14]. For any scene $\mathcal{C} = (C, f)$, let $\mathcal{C}_O$ be the segmentation result (binary scene) output by the given segmentation method for which the ground truth $\mathcal{C}_{gt}$ is known. The three measures of accuracy, FPVF (false positive volume fraction), FNVF (false negative volume fraction), and TPVF (true positive

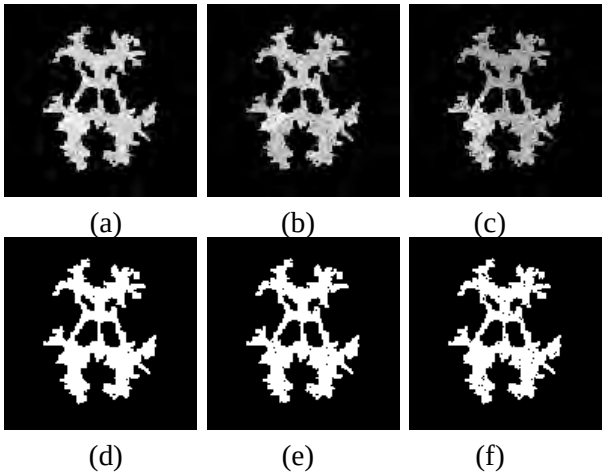

Fig. 4. Connectivity scene and segmented results for the high bias, high noise scene depicted in Fig. 3(b) (contrast level $= 0.5$, bias level $= 10\%$, NCR $= 0.18$, Bias Type IV); (a,d) using the DyW algorithm, (b,e) using the (EqW) algorithm, and (c,f) using the Sqrt algorithm.

volume fraction) are defined as follows:

$$\begin{aligned} \text{FNVF} &= \frac{|\mathcal{C}_{gt} \cap \mathcal{C}'_O|}{|\mathcal{C}_{gt}|} \times 100 \\ \text{FPVF} &= \frac{|\mathcal{C}_O \cap \mathcal{C}'_{gt}|}{|\mathcal{C}_{gt}|} \times 100 \\ \text{TPVF} &= \frac{|\mathcal{C}_O \cap \mathcal{C}_{gt}|}{|\mathcal{C}_{gt}|} \times 100 \end{aligned} \tag{1}$$

Here $|\mathcal{C}_{gt}|$ represents the number of pixels in $\mathcal{C}_{gt}$ with value 1, and the complements of $\mathcal{C}_O$ and $\mathcal{C}_{gt}$ are represented as $\mathcal{C}'_O$ and $\mathcal{C}'_{gt}$, respectively. FNVF indicates the fraction of $\mathcal{C}_{gt}$ missed by the method and FPVF denotes the number of pixels falsely identified by the method, while TPVF denotes the number of pixels correctly identified by the method.

The square region of 5x5 pixels in the lower left lobe of the phantom object shape is considered the seed region for the phantom images. Figure 4 depicts the connectivity scenes and segmented results for high bias field with high noise (contrast level $= 0.5$, bias level $= 10\%$, NCR $= 0.18$, Bias Type IV)(Fig. 3(b)), using the DyW , EqW, and Sqrt algorithms. One can observe how the bias field affects the affinity values in the connectivity map of the EqW algorithm, missing the portion of right upper lobe. The Sqrt algorithm produces higher FNVF as it can not account for intensity variations throughout the image. However, the DyW algorithm for image segmentation assigns higher and consistent affinities across the target region to give more accurate segmentation result.

Figure 5 presents results on accuracy measured in terms of FNVF comparing the DyW algorithm with the EqW and Sqrt algorithms across the range of only one of the image quality parameters. Figure 5(b) clearly depicts the inability of the EqW and Sqrt algorithms to cope with increasing levels of noise. DyW is more accurate across the range on contrast, NCR, and bias levels compared to the other two methods. Figure 6 presents a similar comparison across the ranges of two of the image quality parameters. Figure 7 presents the same data as the first column of Figure 6, but with a different colormap range.

Tables I, II, and III present results on the accuracy of the DyW image segmentation algorithm for phantom images, in terms of FPVF, FNVF, and TPVF. Each cell in Table I corresponds to a particular level of contrast and NCR, and provides the mean and standard deviation of the indicated volume fraction measured over four types and five levels of bias. The values of FPVF and FNVF indicate the decrease in accuracy of the algorithm at the NCR of 18%.In Table II, each cell corresponds to a particular level of bias and contrast, and provides the mean and standard deviation of the indicated volume fraction measured over the same four types of bias and four levels of NCR. The increase in FPVF values indicates decrease in accuracy at high bias and low contrast levels. Finally, in Table III each cell corresponds to a particular level of bias and NCR, and provides the mean and standard deviation of the indicated volume fraction measured over four types of bias and five levels of contrast. This table in conjunction with Tables I and II indicates the high accuracy of the DyW algorithm for the range of image complexities: contrast of $5\% - 65\%$, NCR of up to 14%, and four types of bias with the maximum gain factor of up to 10%.

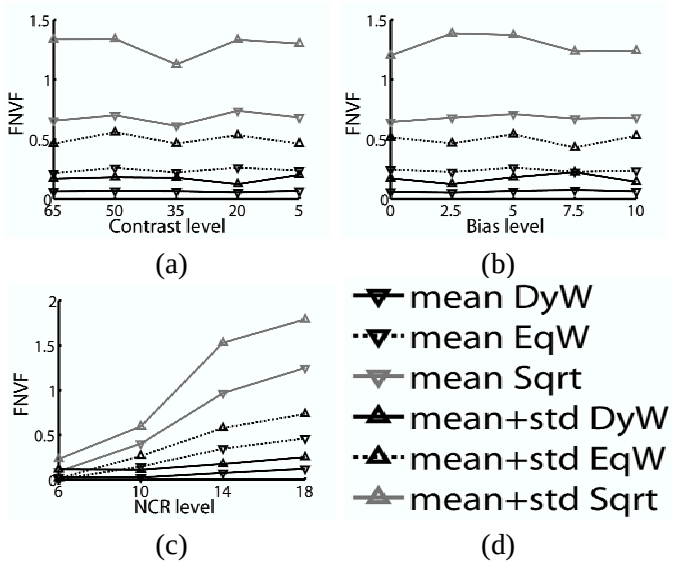

Fig. 5. Accuracy statistics (measured in terms of FNVF) for the DyW algorithm, the EqW algorithm, and the Sqrt algorithm. (a) Statistics for the indicated contrast levels (computed over various NCR and bias levels and types); (b) statistics for the indicated bias levels (computed over various NCR and contrast levels and bias types); (c) statistics for the indicated NCR levels (computed over various contrast and bias levels and types); and (d) legend. All numbers are percentages.

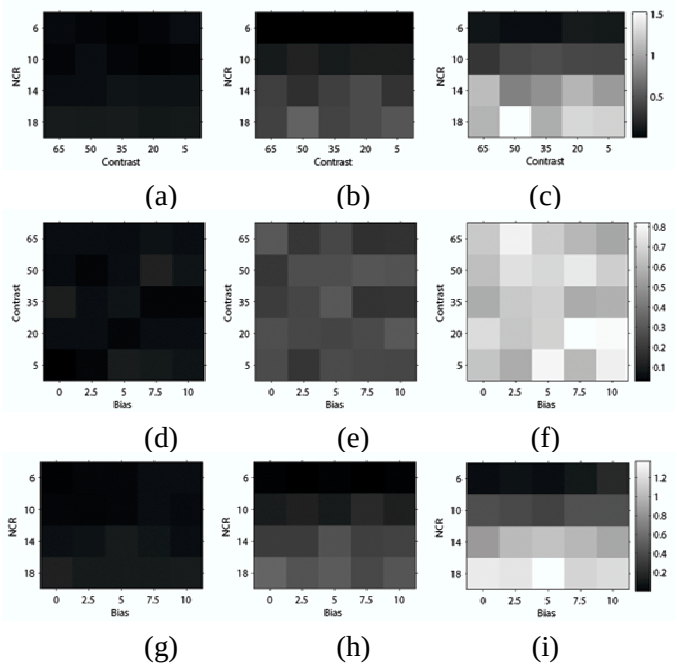

Fig. 6. Accuracy statistics (measured in terms of FNVF) for the DyW algorithm (first column), the EqW algorithm (second column), and the Sqrt algorithm (third column). (a–c) Mean and standard deviation of FNVF for the indicated combinations of NCR and contrast levels (computed over various bias levels and types); (d–f) mean and standard deviation of FNVF for the indicated combinations of contrast and bias levels (computed over various NCR levels and bias types); and (g–i) mean and standard deviation of FNVF for the indicated combinations of NCR and bias levels (computed over various contrast levels and bias types). All numbers are percentages.

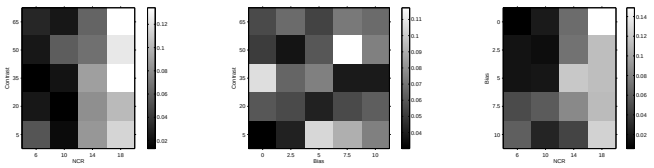

(a) (b) (c)

Fig. 7. Accuracy statistics (measured in terms of FNVF) for the DyW algorithm. (a) Mean and standard deviation of FNVF for the indicated combinations of NCR and contrast levels (computed over various bias levels and types); (b) mean and standard deviation of FNVF for the indicated combinations of contrast and bias levels (computed over various NCR levels and bias types); and (c) mean and standard deviation of FNVF for the indicated combinations of NCR and bias levels (computed over various contrast levels and bias types). All numbers are percentages.

TABLE I

ACCURACY OF THE DYW IMAGE SEGMENTATION ALGORITHM FOR PHANTOM IMAGES, IN TERMS OF FPVF, FNVF, AND TPVF. EACH TABLE ENTRY CORRESPONDS TO A PARTICULAR LEVEL OF CONTRAST AND NCR, AND PROVIDES THE MEAN AND STANDARD DEVIATION OF THE INDICATED VOLUME FRACTION MEASURED OVER FOUR TYPES AND FIVE LEVELS OF BIAS. ALL NUMBERS ARE PERCENTAGES.

Contrast / NCR		6	10	14	18
65	FPVF	0.00 , 0.00	0.00 , 0.00	0.02 , 0.03	0.58 , 0.30
	FNVF	0.03 , 0.10	0.02 , 0.04	0.06 , 0.06	0.13 , 0.16
	TPVF	99.97 , 0.09	99.97 , 0.04	99.94 , 0.06	99.87 , 0.16
50	FPVF	0.00 , 0.00	0.00 , 0.00	0.07 , 0.04	0.69 , 0.35
	FNVF	0.02 , 0.04	0.06 , 0.18	0.07 , 0.07	0.12 , 0.10
	TPVF	99.98 , 0.04	99.94 , 0.18	99.93 , 0.07	99.88 , 0.10
35	FPVF	0.00 , 0.00	0.00 , 0.00	0.02 , 0.04	0.72 , 0.35
	FNVF	0.01 , 0.02	0.02 , 0.02	0.09 , 0.08	0.13 , 0.19
	TPVF	99.99 , 0.02	99.98 , 0.02	99.92 , 0.08	99.87 , 0.19
20	FPVF	0.00 , 0.00	0.00 , 0.00	0.00 , 0.01	0.62 , 0.33
	FNVF	0.02 , 0.03	0.01 , 0.02	0.08 , 0.08	0.10 , 0.08
	TPVF	99.98 , 0.03	99.99 , 0.02	99.92 , 0.08	99.90 , 0.08
5	FPVF	0.00 , 0.00	0.00 , 0.00	0.01 , 0.02	0.89 , 0.50
	FNVF	0.05 , 0.16	0.02 , 0.03	0.09 , 0.17	0.11 , 0.10
	TPVF	99.95 , 0.16	99.98 , 0.03	99.92 , 0.17	99.89 , 0.10

TABLE II

ACCURACY OF THE DYW IMAGE SEGMENTATION ALGORITHM FOR PHANTOM IMAGES, IN TERMS OF FPVF, FNVF, AND TPVF. EACH TABLE ENTRY CORRESPONDS TO A PARTICULAR LEVEL OF BIAS AND CONTRAST, AND PROVIDES THE MEAN AND STANDARD DEVIATION OF THE INDICATED VOLUME FRACTION MEASURED OVER FOUR TYPES OF BIAS AND FOUR LEVELS OF NCR. ALL NUMBERS ARE PERCENTAGES.

Contrast / Bias		0	2.5	5	7.5	10
65	FPVF	0.12 , 0.22	0.15 , 0.35	0.16 , 0.31	0.16 , 0.34	0.14 , 0.24
	FNVF	0.06 , 0.08	0.07 , 0.08	0.05 , 0.06	0.07 , 0.18	0.07 , 0.10
	TPVF	99.95 , 0.08	99.93 , 0.08	99.95 , 0.06	99.93 , 0.18	99.93 , 0.01
50	FPVF	0.23 , 0.43	0.14 , 0.26	0.16 , 0.30	0.15 , 0.30	0.21 , 0.43
	FNVF	0.05 , 0.07	0.04 , 0.05	0.06 , 0.11	0.12 , 0.20	0.07 , 0.07
	TPVF	99.95 , 0.21	99.96 , 0.06	99.94 , 0.100	99.88 , 0.06	99.93 , 0.05
35	FPVF	0.22 , 0.43	0.13 , 0.24	0.17 , 0.34	0.17 , 0.32	0.25 , 0.45
	FNVF	0.11 , 0.21	0.07 , 0.06	0.07 , 0.10	0.04 , 0.06	0.04 , 0.05
	TPVF	99.94 , 0.06	99.95 , 0.09	99.96 , 0.06	99.95 , 0.07	99.98 , 0.08
20	FPVF	0.14 , 0.31	0.13 , 0.28	0.26 , 0.47	0.14 , 0.25	0.12 , 0.25
	FNVF	0.06 , 0.06	0.06 , 0.09	0.04 , 0.06	0.06 , 0.07	0.06 , 0.08
	TPVF	99.97 , 0.05	99.96 , 0.07	99.89 , 0.20	99.91 , 0.18	99.93 , 0.10
5	FPVF	0.24 , 0.46	0.20 , 0.41	0.21 , 0.40	0.35 , 0.70	0.14 , 0.26
	FNVF	0.03 , 0.05	0.04 , 0.07	0.10 , 0.20	0.09 , 0.18	0.07 , 0.10
	TPVF	100.00 , 0.00	100.00 , 0.00	100.00 , 0.01	99.96 , 0.03	99.93 , 0.09

TABLE III

ACCURACY OF THE DYW IMAGE SEGMENTATION ALGORITHM FOR PHANTOM IMAGES, IN TERMS OF FPVF, FNVF, AND TPVF. EACH TABLE ENTRY CORRESPONDS TO A PARTICULAR LEVEL OF BIAS AND NCR, AND PROVIDES THE MEAN AND STANDARD DEVIATION OF THE INDICATED VOLUME FRACTION MEASURED OVER FOUR TYPES OF BIAS AND FIVE LEVELS OF CONTRAST. ALL NUMBERS ARE PERCENTAGES.

NCR / Bias		0	2.5	5	7.5	10
6	FPVF	0.00 , 0.00	0.00 , 0.00	0.00 , 0.00	0.00 , 0.00	0.00 , 0.00
	FNVF	0.01 , 0.01	0.02 , 0.03	0.02 , 0.03	0.05 , 0.16	0.06 , 0.10
	TPVF	99.99 , 0.01	99.98 , 0.03	99.98 , 0.03	99.95 , 0.16	99.94 , 0.10
10	FPVF	0.00 , 0.00	0.00 , 0.00	0.00 , 0.00	0.00 , 0.00	0.00 , 0.00
	FNVF	0.02 , 0.03	0.01 , 0.02	0.02 , 0.03	0.06 , 0.18	0.03 , 0.03
	TPVF	99.98 , 0.03	99.99 , 0.02	99.98 , 0.03	99.94 , 0.18	99.97 , 0.03
14	FPVF	0.02 , 0.04	0.02 , 0.03	0.01 , 0.02	0.02 , 0.03	0.02 , 0.04
	FNVF	0.07 , 0.06	0.07 , 0.08	0.12 , 0.18	0.08 , 0.07	0.04 , 0.05
	TPVF	99.93 , 0.06	99.93 , 0.08	99.88 , 0.18	99.92 , 0.07	99.96 , 0.05
18	FPVF	0.74 , 0.40	0.59 , 0.34	0.75 , 0.32	0.76 , 0.50	0.66 , 0.35
	FNVF	0.15 , 0.18	0.11 , 0.09	0.11 , 0.11	0.11 , 0.16	0.12 , 0.09
	TPVF	99.85 , 0.18	99.89 , 0.09	99.89 , 0.11	99.89 , 0.16	99.88 , 0.09

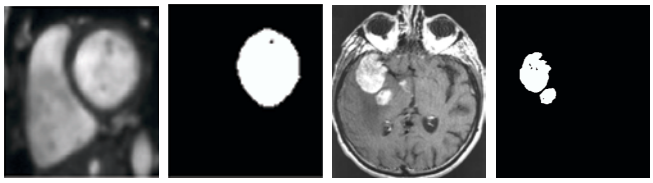

(a) (b) (c) (d)

Fig. 8. Results of the DyW algorithm for (a,b)left ventricular blood pool segmentation in an SSFP and (c,d) lesion segmentation in a T1-weighted MR image, respectively.

We also applied the DyW algorithm to segment MR, CT, and infrared images. In this paper, we present some representative images. The DyW algorithm has been used successfully on cine-MR images for left ventricular (LV) blood segmentation [15]. Representative LV blood pool segmentation in balanced steady state free precession (SSFP) (Figure 8(a,b)) image presents the quality of segmentation achieved in cardiac MR data. Figure 8(c,d) depicts the qualitative segmentation of the right temporal and basal ganglia lesions enhanced strongly with gadolinium in T1-weighted MR images.

The DyW algorithm with multiple seeds has been applied for face segmentation on infrared images. Facial segments in infrared images are typically multi-modal distributions. They feature ‘hot’ and ‘cold’ regions. The ‘hot’ mode regions include the area around the eyes and forehead. The ‘cold’ mode regions include the nose and ears. The multiple seeds are selected on the basis of sharp gradient changes on facial skin. The resulting segmented parts are merged to obtain a complete segmented facial image. We used images from the Equinox database acquired in mid-wave infrared (3-5 microns) for our experiments [16]. Figure 9 depicts representative results of face segmentation using DyW for mid wave infrared images.

(a) (b) (c) (d)

Fig. 9. (b,d) Results of the multi-seed DyW algorithm for face segmentation in the mid-wave infrared images (a,c), respectively.

VI. Conclusion

In this paper we have presented a modification and extension of previously published image segmentation algorithms based on fuzzy-connectedness, which is computed as a linear combination of an object-feature based and a homogeneity based component using fixed weights. Our DyW algorithm introduces directional sensitivity to the homogeneity based component and dynamically adjusts the linear weights in the functional form of fuzzy connectedness.

Various other enhancements of the fuzzy connectedness framework exist. They include attempts in the directions of 1) the adaptivity of affinity components, and 2) obviating the need for thresholding (relative fuzzy connectedness). However, the main contribution of this paper is to the very basic (linear combination of components) formulation of fuzzy connectedness, in terms of adding directional sensitivity to the homogeneity component and a dynamic adjustment of the weights of the affinity components. Dynamic computation of the weights and automatic computation of a threshold relieves the user of an exhaustive search process. This is very critical in applications such as analysis of cardiac cine-MR images, where optimal combination of affinity component weights varies for each slice, each phase, and each subject in spite of data being acquired from the same MR scanner with identical protocol. The intention of this paper is to show that significant improvements can be achieved even in this basic form with our modifications. These modifications, being at the lower level, can be combined with more sophisticated Fuzzy Connectedness methods, such as the vectorial-scale based fuzzy connectedness, which may further improve the segmentation performance. Using the basic form allows us to evaluate the improvements that are due exclusively to our modifications.

The single seed DyW algorithm has been applied successfully to images acquired with different modalities and exhibits accuracy of segmentation within the range of inter and intra–observer variations and a multiple seed approach has been used effectively in infrared face segmentation. Other methods exist that handle the two components of affinity in an adaptive manner, such as Sqrt, however, DyW is more effective in terms of accuracy of segmentation. The DyW image segmentation algorithm consistently achieves accuracy of more than 99.15% for a range of image complexities: contrast 5% to 65%, NCR of 6% to 18% and bias field of different types with the maximum gain factor up to 10%.

References

[1] J. Udupa and S. Samarasekera, "Fuzzy connectedness and object definition: theory, algorithms, and applications in image segmentation," *Graphical Models and Image Processing*, vol. 58, no. 3, pp. 246–261, 1996.

[2] P. Saha, J. Udupa, and D. Odhner, "Scale–based fuzzy connected image segmentation: theory, algorithms, and validation," *Computer Vision and Image Understanding*, vol. 77, pp. 145–174, Apr. 2000.

[3] J. Udupa, L. Nyul, Y. Ge, and R. Grossman, "Multiprotocol MR image segmentation in multiple sclerosis: experience with over 1,000 studies," *Academic Radiology*, vol. 8, no. 11, pp. 1116–1126, Nov. 2001.

[4] A. S. Pednekar, I. A. Kakadiaris and U. Kurkure, "Adaptive fuzzy connectedness–based medical image segmentation," in *Proc. Indian Conference on Computer Vision, Graphics, and Image Processing (ICVGIP)*, Ahmedabad, India, Dec. 2002, pp. 457–462.

[5] L. A. Zadeh, "Fuzzy sets," *Information and Control*, vol. 8, no. 3, pp. 338–353, 1965.

[6] A. Rosenfeld, "Fuzzy digital topology," *Information and Control*, vol. 40, no. 1, pp. 76–87, Jan. 1979.

[7] A. Rosenfeld, "On connectivity properties of grayscale pictures," *Pattern Recognition*, vol. 16, no. 1, pp. 47–50, 1983.

[8] I. Bloch, "Fuzzy connectivity and mathematical morphology," *Pattern Recognition Letters*, vol. 14, no. 6, pp. 483–488, 1993.

[9] S. Dellepiane and F. Fontana, "Extraction of intensity connectedness for image processing," *Pattern Recognition Letters*, vol. 16, pp. 313–324, 1995.

[10] P. Saha and J. Udupa, "Relative fuzzy connectedness among multiple objects: theory, algorithms, and applications in image segmentation," *Computer Vision and Image Understanding*, vol. 82, pp. 42–56, 2000.

[11] P. Saha and J. Udupa, "Fuzzy connected object delineation: Axiomatic path strength definition and the case of mulitiple seeds," *Computer Vision and Image Understanding*, vol. 83, pp. 275–295, 2001.

[12] P. Saha and J. Udupa, "Tensor scale–based fuzzy connectedness image segmentation," in *Proc. SPIE Medical Imaging: Image Processing*, vol. 5032, San Diego, CA, 2003, pp. 1580–1590.

[13] N. Otsu, "A threshold selection method from gray-level histograms," in *IEEE Transactions on Systems, Man, and Cybernetics*, vol. 9, no. 1, Jan. 1979, pp. 62–66.

[14] J. Udupa, V. LaBlanc, H. Schmidt, C. Imielinska, P. Saha, G. Grevera, Y. Zhuge, L. Currie, P. Molholt, and Y. Jin, "Methodology for evaluating image segmentation algorithms," in *Proc. SPIE Medical Imaging*, vol. 4684, no. 1, 2002, pp. 266–277.

[15] A. Pednekar, I. Kakadiaris, U. Kurkure, R. Muthupillai, and S. Flamm, "Validation of automatic computation of ejection fraction," in *Proc. Medical Image Computing and Computer-Assisted Intervention (MICCAI)*, Nov. 2003, p. 987.

[16] P. Buddharaju, I. Pavlidis, and I. Kakadiaris, "Face recognition in the thermal infrared spectrum," in *Proc. Joint IEEE International Workshop on Object Tracking and Classification Beyond the Visible Spectrum*, Washington, DC, June 2004.